JOURNAL OF GUIDANCE, CONTROL, AND DYNAMICS
Vol. 33, No. 6, November–December 2010

Engineering Notes

Control Model for Robotic Samara: Dynamics About a Coordinated Helical Turn

Evan R. Ulrich,* Imraan Faruque,* Jared Grauer,*
Darryll J. Pines,† J. Sean Humbert,‡ and James E. Hubbard Jr.§
University of Maryland, College Park, Maryland 20742

DOI: 10.2514/1.50878

Nomenclature

F_{CF}	=	centrifugal force
F_G	=	gravity force
F_P	=	propulsive force
F_{W_D}	=	drag force
F_{W_L}	=	lift force
$L(y)$	=	lift per unit length, N/m
m	=	mass of robotic samara, kg
$m(y)$	=	mass per unit length, kg/m
m_w	=	mass of wing, kg
p, q, r	=	rotational velocities, rad/s
R	=	length of wing
r_{turn}	=	virtual-body turn radius, m
$s(\hat{\theta})$	=	standard error
t	=	time, s
u, v, w	=	translational velocities, m/s
$\dot{w}$	=	heave acceleration, m/s^2
x, y, z	=	inertial frame position, m
$\beta_0, \beta_{1c}, \theta_0$	=	wing and disk orientation angles, deg
γ	=	flight-path angle, rad
γ_l	=	lock number
θ_0	=	control input
λ_i	=	uniform inflow
ϕ, θ, ψ	=	Euler angles, rad
$\dot{\psi}_{cg}$	=	virtual-body turn rate, rad/s
Ω	=	rotation rate, rad/s

I. Introduction

THIS Note details the flight dynamics and control of a prototype monowing rotorcraft that mimics the passive transit of the species of samara (winged seed), *Acer diabolicum Blume*. The asymmetric and all-rotating platform requires the development of a novel sensing and control framework. An approach to directional control that does not require the once-per-revolution actuation or high-frequency measurement of vehicle orientation is demonstrated for the first time. In flight, the vehicle's differing responses to impulsive and step inputs are leveraged to create a control strategy that provides full controllability. The general rigid-body dynamics are separated into rotor dynamics and particle navigation, which are derived for a coordinated helical turn flight path. The equations of motion are used to calculate the forces necessary for flight along a trajectory recorded with a visual motion capture system. The result is a framework for state estimation and control, applicable to scaled versions of the robotic samara.

In recent years a new paradigm of flight has emerged encompassing microscale bioinspired aircraft. These highly maneuverable platforms are capable of hovering flight and are ideally suited for operation in a confined environment. The reconnaissance mission envisioned requires a high level of autonomy, due to the fast dynamics of the vehicle and the limit on communication in the likely areas of operation: e.g., caves and buildings. Development of the equations of motion about a trimmed-flight condition will facilitate future model-based controller and observer design, enabling autonomous operation.

Aerial systems that satisfy the dimensional constraints outlined by the Defense Advanced Research Projects Agency's Nano Air Vehicle (NAV) initiative [1] include fixed-wing, rotary-wing, and flapping-wing vehicles. The simplest and most mature of these platforms are fixed-wing vehicles, which boast speed, simplicity, and well-known dynamics; however, the necessity for forward flight restricts functionality in cluttered environments that can be traversed by rotary and flapping-wing platforms.

A substantial challenge in modeling the dynamics of microscale flight is the general lack of knowledge of the complex low Reynolds number flow regime they inhabit. The inherently three-dimensional flow of rotary-wing vehicles cannot be adequately modeled using two-dimensional airfoil data, as lift production at this scale exceeds prediction [2]. The complexity of the system can be reduced substantially by identifying a linear model that describes its reaction to forces imposed by a control input. A model description of this nature lends itself well to modern control and state estimation.

This Note characterizes the forward-flight dynamics and control of a rotary-wing NAV based on one of nature's most efficient fliers: the seed of the maple (*Acer*) tree or samara. The work begins with a description of the vehicle and experimental setup. Then recorded flight tests are shown and the characteristics of the flight path are analyzed. Next, the rigid-body dynamics are derived for a flight path consisting of a helical turn. The equations of motion are then linearized about a trimmed-flight condition, from which the small perturbation equations of motion can be expressed in canonical state-space form. Equation-error and output-error methods are used to compute parameter estimates from flight data. The result of this work is a framework for state estimation and control.

II. Materials and Methods

A. Monocopter Description

The concept of a single-wing rotating aircraft is not a new one; in fact, the first vehicle of this type was flown in 1952 in the woods surrounding Lake Placid, New York [3]. A more recent vehicle was developed and flown by a team led by Lockheed Martin Advanced Technology Laboratories [4]. The prototype called MAVPro incorporated an outrunner motor with an 8-in.-diam propeller, weighed 0.514 kg, rotated at a stable 4 Hz, and could climb to 50 ft with radio-controlled actuation of a trailing-edge flap. The MAVPro incorporated the AG38 airfoil and exhibited a rectangular planform geometry. The various single-winged rotating aircraft developed over the years have made no attempt to use the most basic mode of

Presented at the 2010 American Control Conference, Baltimore, MD, 30 June–2 July 2010; received 21 May 2010; revision received 22 July 2010; accepted for publication 25 July 2010.

*Graduate Student, Department of Aerospace Engineering. Member AIAA.
†Professor, Aerospace Engineering; Dean of Engineering, A. James Clark School of Engineering. Fellow AIAA.
‡Assistant Professor, Department of Aerospace Engineering. Member AIAA.
§Langely Distinguished Professor, Department of Aerospace Engineering. Associate Fellow AIAA.

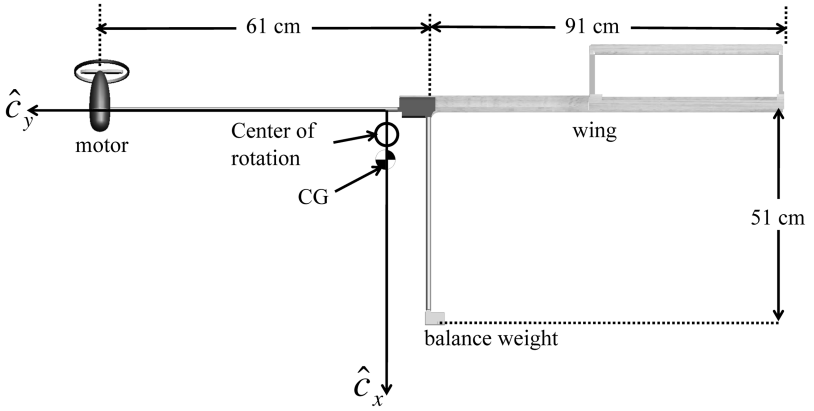

Fig. 1 Conventional monocopter schematic [3].

transit of natural samara: autorotation. Additionally, airfoil cross sections and planform designs have had no similarity to those found in natural samaras.

Conventional monocopter designs apply torque to the vehicle with a thrust device slightly offset from the $\hat{c}_y$ axis (see Fig. 1), and in the case of MAVPro, the propeller spins in the $\hat{c}_y$-$\hat{c}_z$ plane and influences the stability about the $\hat{c}_y$ axis. This configuration results in the propeller fighting the pitch input from the flap and reduces controllability of the vehicle. The 3.5-in.-diam propeller of the robotic samara is spinning in the $\hat{c}_x$-$\hat{c}_z$ plane and opposes applied torque about the $\hat{c}_x$ axis, providing additional roll stability. The configuration of the robotic samara permits control of rotation rate, altitude, and translation via the appropriate actuation of the wing servo. The component layout and sign convention of the vehicle used in this study are shown in Fig. 2.

The vehicle detailed in this study is a type of monowing rotorcraft modeled after the species of samara *Acer diabolicum Blume*. The layout of the vehicle consists of two rigid bodies linked by a servo allowing one rotational degree of freedom. The first rigid body and main lifting surface resemble a scaled version of a samara, both in planform geometry and airfoil cross section [5–7]. The second rigid body houses the electronics and motor/propeller unit, applying a torque to rotate the vehicle as required for flight (Fig. 2). The body-fixed axis $[\hat{c}_x, \hat{c}_y, \hat{c}_z]$ and Euler angles $[\phi_w, \theta_w, \psi_w]$ describe the orientation of the vehicle, which is shown in Fig. 2, along with the dimensions of the vehicle.

Flight of a monocopter differs from full-scale helicopters, as there is no stationary frame of reference from which control inputs can be applied: i.e., helicopter swashplate. Control of the vehicle with once-per-revolution inputs requires knowledge of the vehicle's orientation relative to the desired flight path, but sensor packages capable of recording onboard flight data at the rate necessary for this type of control are not commercially available in the weight class required for use on nano-class vehicles. Instead, control algorithms development is based on state information collected externally using a visual-motion capture system. This approach has been successful in identifying the pitch and heave dynamics of a similar vehicle, which is described in [7]. An approach to directional control that does not require the once-per-revolution actuation or high-frequency measurement of vehicle orientation is discussed in detail in this Note.

B. Open-Loop Flight-Test Experimental Setup

Position and orientation of each vehicle was collected at a rate of 500 Hz using a visual tracking system.

III. Flight Dynamics Model

A. Virtual-Body Model

For the purposes of guidance, navigation, and control, a traditional manned aerial vehicle has a set of six–seven configuration variables corresponding to the 3-D position of the center of gravity, and the remaining three–four are used to describe the orientation of the vehicle relative to an inertial reference frame. For the robotic samara, the body orientation evolves over time, ranging from a steady rotation rate about the $\hat{i}_z$ axis in hover to more complex pitching, rolling, flapping, and rotating motions in other flight conditions, such as the translational flight condition addressed in the study.

To simplify the description, consider instead the disk described by the motion of the wingtip over each revolution, or tip path plane (TPP). As defined in traditional rotorcraft analysis, the TPP considered is one that discards the harmonic motion higher than

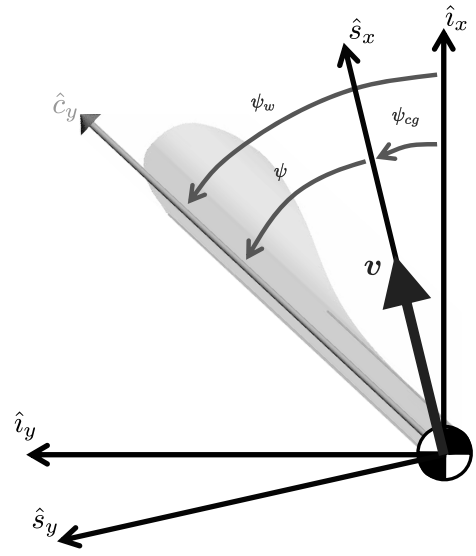

Fig. 2 Definition of azimuth angles of the wing ψ_w, virtual body ψ_{cg}, and virtual body with respect to the wing ψ.

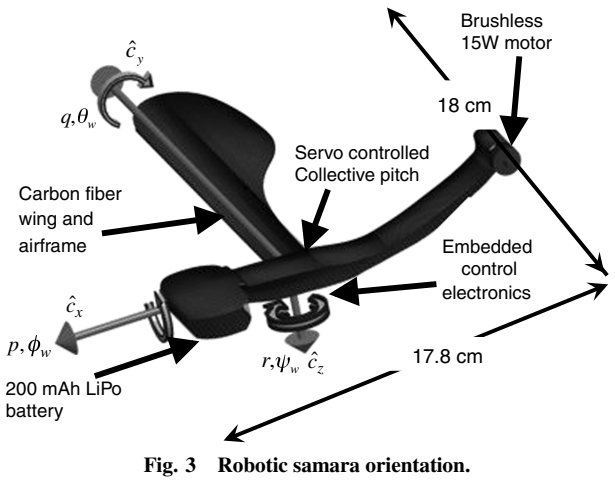

Fig. 3 Robotic samara orientation.

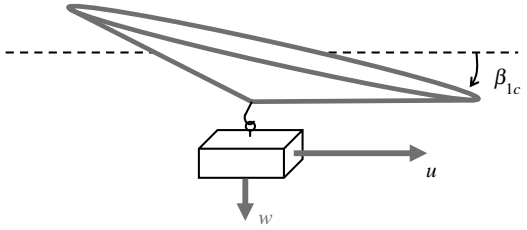

Fig. 4 Modeling the samara as a rotor with a hinged virtual body.

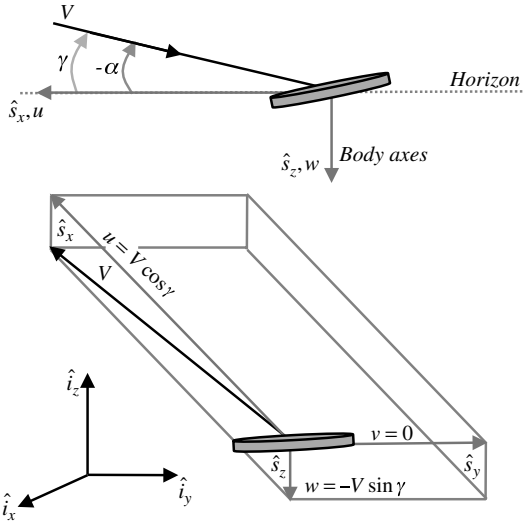

Fig. 5 Definition of angle of attack and sideslip angle in relation to the velocity components.

1/rev, allowing a plane to be defined from the surface. The aerodynamic lift force may be considered to act perpendicularly to the TPP.

To describe the dynamics of the samara, consider a virtual (rigid) body connected to the disk center with an ideal hinge, with its center of gravity located directly below the disk center, and with the mass of the samara, as shown in Figs. 2 and 3. No aerodynamic moments may be transmitted across an ideal hinge, splitting the position/orientation dynamics into *rotor dynamics* describing the flapping motion of the blade and into *positional dynamics* of the samara to be described using the translational equations of motion for the motion of a point mass acted upon by the rotor disk forces.

The forward flight of the vehicle is most conveniently formulated in a nonrotating frame of reference attached to the virtual body. The orientation of the virtual-body forward velocity u is defined by the projection of the velocity vector onto the $[\hat{i}_x, \hat{i}_y]$ plane so that translation can only occur in the u direction and $v = 0$. The heave velocity is parallel to the inertial $\hat{i}_z$ axis and is shown in Fig. 5. Also shown are the equal and opposite definitions of aerodynamic incidence α and the flight-path angle γ in relation to the virtual-body velocities u and w. The cyclic blade flapping is defined as the angle between the wing and the inertial plane $[\hat{i}_x, \hat{i}_y]$ and is shown in Fig. 6:

$$[u, v, w]^T = [V\cos\gamma, 0, -V\sin\gamma]^T \tag{1}$$

B. Equations of Motion for a Flapping Blade

In steady hovering flight the coning angle $\beta = \beta_0$ is constant and is independent of ψ. In forward flight the cyclically varying airloads induce an additional flapping response that varies about the azimuth ψ. The aerodynamic, centrifugal, and inertial forces acting on the robotic samara wing determine the observed coning angle (Fig. 6).

We define a positive moment as one that acts to reduce the β. The centrifugal force can then be written for an element along the span as

$$\mathrm{d}(M_{\mathrm{CF}}) = (m_w(y)\,\mathrm{d}y)y^2\Omega^2\beta = m_w(y)y^2\Omega^2\beta\,\mathrm{d}y \tag{2}$$

and the inertial moment about the flap hinge as

$$\mathrm{d}(I) = (m_w(y)\,\mathrm{d}y)y^2\ddot{\beta} = m_w(y)y^2\ddot{\beta}\,\mathrm{d}y \tag{3}$$

Additionally, the aerodynamic moment is

$$\mathrm{d}(M_\beta) = -L(y)y\,\mathrm{d}y \tag{4}$$

The aerodynamic force on a blade element with chord c, and distance y from the rotational axis can be calculated using blade element theory under the assumption of uniform inflow [8]. With these considerations, the aerodynamic moment about the flap hinge can be shown to be

$$\int_0^R Ly\,\mathrm{d}y = \frac{1}{8}\rho\Omega^2 cCl_\alpha R^4\left(\theta_0\frac{\dot{\beta}}{\Omega} - \frac{4\lambda_i}{3}\right) \tag{5}$$

The equation of motion can then be written as the sum of all the moments:

$$\int_0^R m_w(y)y^2\Omega^2\beta\,\mathrm{d}y + \int_0^R m_w(y)y^2\ddot{\beta}\,\mathrm{d}y + \int_0^R -Ly\,\mathrm{d}y \tag{6}$$

The mass moment of inertia of the wing about the flap hinge is

$$I_b = \int_0^R m_w(y)y^2\,\mathrm{d}y \tag{7}$$

so that the equation of motion simplifies to

$$I_b\ddot{\beta} + I_b\Omega^2\beta = \int_0^R Ly\,\mathrm{d}y \tag{8}$$

The sum of the applied moments form the differential equation describing the blade flapping motion. The flap equation can be written as a function of azimuth angle instead of time, where $\psi = \Omega t$ results in the following transformation: $\dot{\beta} = \Omega\overset{*}{\beta}$ and $\ddot{\beta} = \Omega^2\overset{**}{\beta}$. The equation of motion of the robotic samara flapping wing reduces to

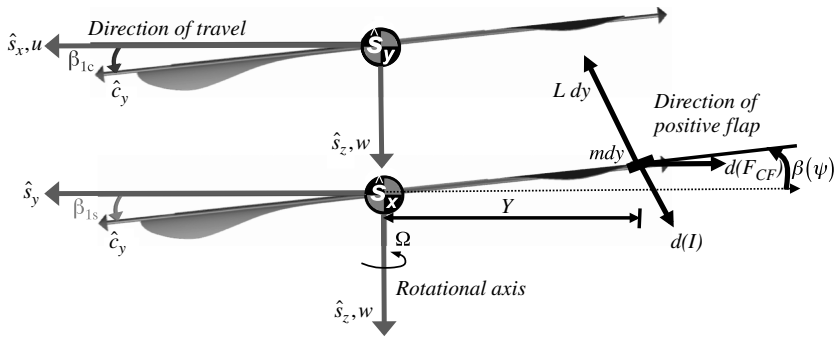

Fig. 6 Definition of coning angles β_{1s} and β_{1c} with forces acting on an element of a flapping robotic samara wing.

Table 1 Robotic samara wing properties

Measurement	Symbol	Value	Unit
Air density	ρ	1.225	kg/m^3
Mean chord	c	3.5	cm
Wing length	R	18	cm
Lift-curve slope	$C_{l\alpha}$	3.5	——
Wing inertia	I_b	23.3μ	kg · m^2

$$\overset{**}{\beta} + \frac{\gamma_l}{8}\overset{*}{\beta} + \beta = \frac{\gamma_l}{8}\left[\theta - \frac{4}{3}\lambda_i\right] \tag{9}$$

where γ_l is the lock number of the robotic samara. The lock number is a function of the aerodynamic and geometric parameters listed in Table 1 and is computed as

$$\gamma_l = \frac{\rho C l_\alpha c R^4}{I_b} = 6.75 \tag{10}$$

The lift-curve slope Cl_α was calculated from a combined blade element and momentum theory model of the robotic samara in hover. The kinematics of the model were based on flight tests of the vehicle in hover, and the presented value of Cl_α adequately captures the hover performance of the robotic samara. However, in the analysis that follows, the value of γ_l and Cl_α are not required and parameter estimates do not take these values into account.

Detailed numerical and steady-state analytic solutions for the flap equation (9) have demonstrated good agreement with a first-order harmonic series [8]. Harmonic analysis of the flap equation allows a periodic solution of the form

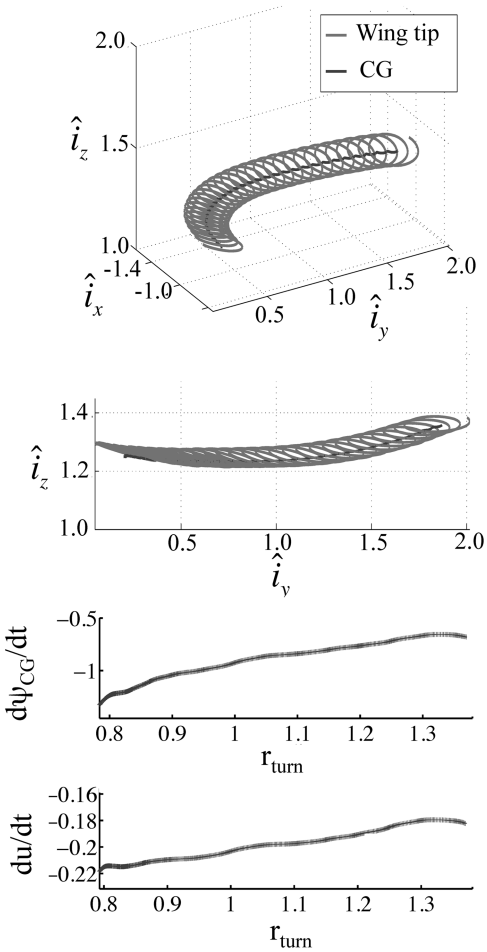

Fig. 7 Flight data for a steady helical turn, including turn radius r_{turn} and turn rate $\dot{\psi}_{cg}$.

$$\beta = \beta_0 + \beta_{1s}\sin(\psi) + \beta_{1c}\cos(\psi) \tag{11}$$

The blade flapping throughout the u turn is observed to be periodic with respect to the azimuth angle ψ. The periodic coefficients describe the direction of force and can be seen to correlate with both the velocity and acceleration of the virtual body in Fig. 7. The β_{1c} term influences the magnitude of u, and the β_{1s} term influences the magnitude $\|\mathbf{V}_{cg}\|$.

The coefficients β_{1s} and β_{1c} are the out-of-plane flapping angles that describe the orientation of the wing within the disk. The orientation of the virtual body defines the roll and pitch angles to be $\phi = \beta_{1s}$ and $\theta = \beta_{1c}$, respectively. Thus, the flapping of the wing in forward flight describes the instantaneous orientation of the virtual body, which includes the coning angle β_0.

C. Rigid-Body Equations of Motion

The rigid-body equations of motion are differential equations that describe the evolution of the state variables subject to applied forces. In body-fixed axes, the sum of all external forces applied to the center of gravity is

$$m\dot{\mathbf{V}}_{cg} + mS(\boldsymbol{\omega})\mathbf{V}_{cg} = \mathbf{f} \tag{12}$$

where m is the vehicle mass; $\mathbf{V}_{cg} = u\hat{s}_x + v\hat{s}_y + w\hat{s}_z$ is the translational velocity of the center of gravity; $\boldsymbol{\omega} = p\hat{s}_x + q\hat{s}_y + r\hat{s}_x$ are the body-fixed roll, pitch and yaw rates; $\mathbf{f} = f_x\hat{s}_x + f_y\hat{s}_y + f_z\hat{s}_z$ are externally applied forces; and $S(.)$ is a skew operator.

The rotational dynamics are governed by the differential equation:

$$\mathbf{I}\,\dot{\boldsymbol{\omega}} + S(\boldsymbol{\omega})\mathbf{I}\boldsymbol{\omega} = \boldsymbol{\tau} \tag{13}$$

where $\boldsymbol{\tau}$ is a vector of externally applied torques and $\mathbf{I}$ is a diagonal inertia matrix arising from symmetries in the virtual aircraft.

D. Coordinated Helical Turn

The flight path of the vehicle resembles a steady banked turn such that $\dot{\phi}_0$ and $\dot{\theta}_0$ are equal to zero. Additionally, the flight-path angle γ is small (greater than 0 for climbing flight) so that $\sin\gamma = \gamma$ and $\cos\gamma = 1$. The kinematic equations are then

$$p = -\dot{\psi}_{cg}\sin\beta_{1c} \tag{14}$$

$$q = \dot{\psi}_{cg}\cos\beta_{1c}\sin\beta_{1s} \tag{15}$$

$$r = \dot{\psi}_{cg}\cos\beta_{1c}\cos\beta_{1s} \tag{16}$$

Substituting the derived velocities and modified kinematics into the force equilibrium equations results in the following equations of motion:

$$X = mg\sin\beta_{1c} + m(\dot{u} + wq - vr) \tag{17}$$

$$Y = -mg\cos\beta_{1c}\sin\beta_{1s} + m(\dot{v} + ur - wp) \tag{18}$$

$$Z = -mg\cos\beta_{1c}\cos\beta_{1s} + m(\dot{w} + vp - uq) \tag{19}$$

where $[X, Y, Z]^T$ represent force equilibrium in the body-fixed coordinate frame, and g is acceleration due to gravity.

Flight tests conducted with the robotic samara provide a means of verifying the equations of motion. A portion of a flight that fits within the constraints of the proposed analytical model is shown in Fig. 7.

The variation of $\dot{\psi}_{cg}$ with the turn radius r_{turn} is observed to be linear for most of the trial, where a small but linear change in r_{turn} corresponds to a large change in turn rate $\dot{\psi}_{cg}$. The final portion of the figure shows the linear change in forward-speed derivative $\dot{u}$ with respect to r_{turn}.

E. Extension to Forward Flight

1. Pure Longitudinal Motion

Consider now straight flight as a special case of a coordinated turn, where $\dot{\psi} = p_0 = q_0 = r_0 = \beta_{1s} = 0$. The equation of motion along the $\hat{s}_x$ axis for forward flight may be written as the combination of a nominal condition (represented by $[\,]_0$) and a small perturbation $\Delta[\,]$ as

$$X_0 + \Delta X - mg[\sin(\beta_{1c0}) + \Delta\beta_{1c}\cos(\beta_{1c0})] = \Delta\dot{u} \tag{20}$$

Setting all perturbation quantities to zero ($\Delta[\,] = 0$) yields the force equilibrium along trimmed forward flight:

$$\frac{X_0}{m} = g\sin\beta_{1c0} \tag{21}$$

2. Perturbation Equations

The trimmed forward-flight equation (21) can be subtracted from the linearized force equilibrium equation (20), leading to a description of small perturbation motion about the equilibrium condition as

$$\Delta\dot{u} = \Delta X - mg\Delta\beta_{1c}\cos\beta_{1c} \tag{22}$$

Separating out the linear effects of the longitudinal variables $[u, w, \beta_0, \beta_{1c}]$ facilitates development of a canonical linear control model and can be written as

$$\frac{\Delta X}{m} = X_u\Delta u + X_w\Delta w + X_{\beta_0}\Delta\beta_0 + X_{\beta_{1c}}\Delta\beta_{1c} + \frac{X_c}{m} \tag{23}$$

where $X_{[\cdot]} = (1/m)\partial X/\partial[\cdot]$, and

$$\frac{\Delta X_c}{m} = X_\theta\Delta\theta \tag{24}$$

The time-invariant linear system can now be expressed in state-space form $\dot{\mathbf{x}} = \mathbf{A}\mathbf{x} + \mathbf{B}\mathbf{u}$, where $\mathbf{x} = [\Delta u, \Delta w, \Delta\beta_0, \Delta\beta_{1c}]^T$, and $\mathbf{u} = [\Delta\theta_0]$. Dropping the $[\Delta]$, the state-space model is written in matrix form as

$$\begin{bmatrix} \dot{u} \\ \dot{w} \\ \dot{\Omega} \\ \dot{\beta}_0 \\ \dot{\beta}_{1c} \end{bmatrix} = \begin{bmatrix} X_u & X_w & 0 & 0 & 0 \\ 0 & 0 & Z_\Omega & Z_{\beta_0} & 0 \\ 0 & 0 & \Omega_\Omega & \Omega_{\beta_0} & 0 \\ 0 & 0 & \beta_{0\Omega} & 0 & 0 \\ \beta_{1cu} & 0 & \beta_{1c\Omega} & \beta_{1c\beta_0} & 0 \end{bmatrix} \begin{bmatrix} u \\ w \\ \Omega \\ \beta_0 \\ \beta_{1c} \end{bmatrix} + \begin{bmatrix} X_{\theta_0} \\ Z_{\theta_0} \\ 0 \\ \beta_{0\theta_0} \\ 0 \end{bmatrix} \theta_0 \tag{25}$$

IV. Experimental Results

Position and orientation of each vehicle was collected at a rate of 500 Hz using a visual tracking system. The open-loop control setup used to pilot the vehicle and record vehicle state information is discussed in [7]. During a flight test, the tracking system uses eight cameras to track the three-dimensional position of three retroreflective markers placed on the samara wing. A model of the vehicle geometry and the exact locations of the markers are used for least-squares estimates of the position of the center of gravity as well as orientation. The open-loop control setup and measurement noise characteristics are detailed in [7]. The obtained position estimates are exceptionally low noise as compared to commercial-grade onboard attitude estimation sensors. The position noise variance was estimated by recording data while not moving the vehicle. The low noise presence in the position estimate allows the inertial position to be numerically differentiated, using a central difference scheme, to yield inertial velocity estimates.

Lateral directional flight was recorded in the laboratory for a flight path consisting of an initial trim state and a perturbation about the trim (Fig. 8). In general, the turn radius is inversely proportional to the collective pitch of the wing. While an impulsive response input changes the heave velocity of the vehicle, a step input changes the turn radius of the flight path. The samara travels in the opposite direction of the motion that would be induced by an impulsive collective input applied at that instant. The finding that the step response spends part of its time going in the wrong direction is an indication of a nonminimum phase system, or a right-half-plane zero, and the vehicle's differing responses to impulsive and step inputs are leveraged to create a control strategy that provides full controllability, where an alternating series of large and small turn radii can be used to steer the vehicle in a specific direction. While a right-half-plane zero is normally a performance limitation, in this case, the behavior that typically restricts performance has been used in the control strategy to enable a single input to control multiple degrees of freedom.

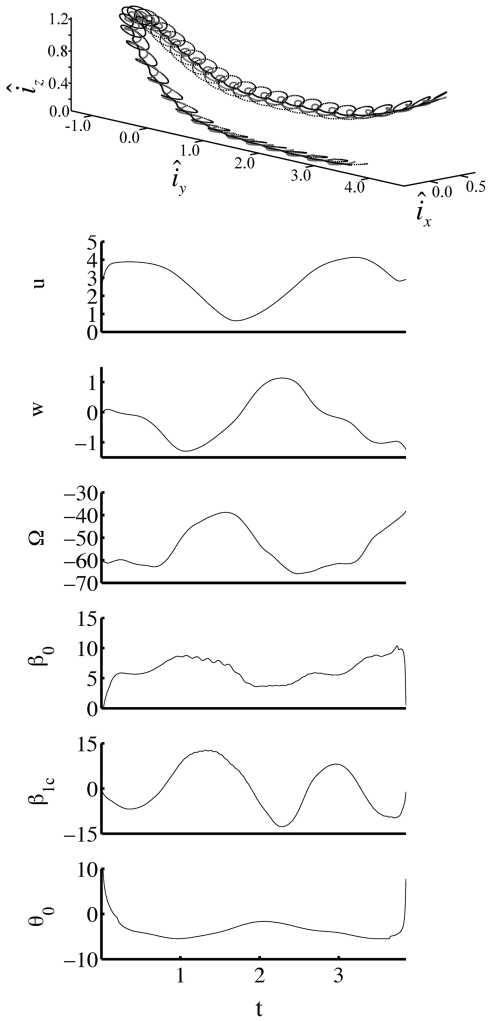

Fig. 8 State trajectories in a coordinated turn.

Table 2 Parameter estimates and standard errors

Parameter	Equation error	Output error
θ	$\hat{\theta} \pm s(\hat{\theta})$	$\hat{\theta} \pm s(\hat{\theta})$
X_u	$+0.4165 \pm 0.1753$	$+0.8978 \pm 0.3416$
X_w	$+3.7378 \pm 0.5694$	$+1.6108 \pm 0.4431$
X_{θ_0}	-7.9875 ± 21.055	$+114.35 \pm 25.827$
Z_Ω	$+0.2538 \pm 0.0164$	$+0.2237 \pm 0.0318$
Z_{β_0}	-57.323 ± 12.301	-17.695 ± 23.318
Z_{θ_0}	-14.718 ± 13.399	$+38.942 \pm 19.449$
Ω_Ω	-1.3358 ± 0.2084	-2.2649 ± 0.5876
Ω_{β_0}	$+1001.5 \pm 63.791$	$+1231.1 \pm 219.49$
$\beta_{0\Omega}$	-0.0081 ± 0.0008	-0.0063 ± 0.0008
$\beta_{0\theta_0}$	-1.8922 ± 0.3399	-2.3455 ± 0.3158
β_{1cu}	-0.5881 ± 0.2122	$+0.5628 \pm 0.2050$
$\beta_{1c\Omega}$	-0.1145 ± 0.0325	$+0.0872 \pm 0.0540$
$\beta_{1c\beta_0}$	$+24.323 \pm 7.7405$	-22.543 ± 15.787

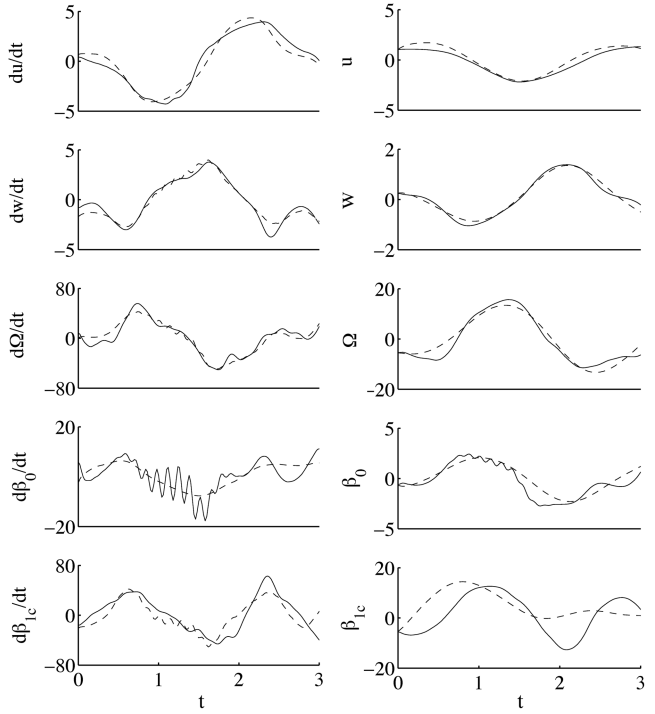

Fig. 9 Equation-error and output-error model fit to perturbation data. Measurements are plotted with the solid line, and model outputs are plotted with a dashed line.

The velocity components, rotation rate, and blade flap angles are shown in Fig. 8 as they vary with the input θ_0. The first 0.5 s of flight correspond to a near-constant u and near-zero w. At the time of the u turn, 1–1.5 s, there is an increase in the vertical velocity. The increase is correlated because a collective pitch increase used to change the heave velocity is also used to change the flight-path direction.

The flight data shown in Fig. 8 were used to perform system identification using algorithms implemented in a MATLAB toolbox called System Identification Programs for Aircraft, detailed in [9]. Guided by analytical modeling, modified stepwise regression was used to determine the model structure using the statistical significance of measured states, resulting in the system shown in Eq. (25). This model structure was chosen to maximize the model fit using regressors with a significant partial-f ratio, while minimizing the parameter estimate error bounds. A two-step procedure using the equation-error method, followed by the output-error method, was used to estimate the stability derivatives in the model. The equation-error method performs a linear estimation at the acceleration level, which has a deterministic solution that is inexpensive to compute. The output-error method, widely regarded as more accurate, performs a nonlinear estimation at the level at which measurements were taken. This method requires an iterative numerical solver, but initial guesses using an equation-error estimate typically converge quickly. Parameter estimates and standard errors corrected for non-white colored residuals are given in Table 2. Model fits to the perturbation data sets are shown in Fig. 9 for the equation-error and output-error methods, where the measurements are plotted with a solid line and the model outputs are plotted with a dashed line.

The model structure and parameter estimates fit the data well in most cases. In the case of $\mathrm{d}\beta_0/\mathrm{d}t$ the model failed to capture the higher-frequency content, which may be due to nonlinear or multi-body effects not captured in the linearized model. The equation-error results had model fits of 0.94, 0.94, 0.91, 0.56, and 0.59 for matching $\dot{\mathbf{x}}$ measurements and fits of 0.85, 0.97, 0.92, 0.83, and 0.12 for matching $\mathbf{x}$ measurements. The equations describing the flap dynamics had low model fits for both methods. Several parameters were estimated consistently by the two methods, lying within two standard deviations of each other. However, several estimates did not match well and had large error bounds. These inconsistencies are due to limited excitation present in the flight data and will be remedied in the future with flight tests that are better suited for system identification.

V. Conclusions

This Note presents the derivation of the equations of motion of a robotic samara designed and constructed at the University of Maryland. An approach to directional control that does not require the once-per-revolution actuation or high-frequency measurement of vehicle orientation has been demonstrated for the first time. Lateral flight is attained through the vehicle's differing responses to impulsive and step inputs that are leveraged to create a control strategy that provides full controllability. The nonlinear Euler equations were used to describe the rigid-body dynamics of the vehicle in a steady turn and are then extended to forward flight and linearized about a trim state, resulting in five linearized small perturbation equations in state-space form. Flight tests provided high-accuracy position information, which was reduced to wing flap angles and virtual-body velocities, was used to specify a flight condition that fit within the limits of the derived model and allowed for estimation of the vehicles' stability derivatives. The dynamics of the robotic samara during a coordinated turn can be approximated by a linearized model. Future work will validate the model structure and give physical significance to model parameters.

Additionally, several linear relationships were shown to exist, including $[r_{\text{turn}}, \dot{u}]$ and $[r_{\text{turn}}, \dot{\psi}]$. The steady turn discussed here has been observed in scaled versions of the robotic samara. Therefore, the open-loop control demonstrated and analyzed is considered to be appropriate for similar vehicles of reduced size with limited sensing and actuation capabilities.

Acknowledgments

This work was funded by the A. James Clark School of Engineering. Flight tests were conducted at the University of Maryland. The authors would like to acknowledge support from the University of Maryland and would like to thank the members of the Autonomous Vehicle Laboratory and the Morpheus Laboratory for their continued teamwork and motivation.

References

[1] "Defense Sciences Office Nano Air Vehicle," DARPA, TR W31P4Q-06-C-0324, Sept. 2009.

[2] Pines, D., and Bohorquez, F., "Challenges Facing Future Micro-Air-Vehicle Development," *Journal of Aircraft*, Vol. 43, No. 2, 2006, pp. 290–305. doi:10.2514/1.4922

[3] Graham, F., *Monocopters*, Perigee, East Liverpool, OH, 1999, p. 24.

[4] Jameson, S., Allen, N., and Youngren, H., "SAMARAI Nano Air Vehicle—A Revolution in Flight," DARPA CR W31P4Q-06-C-0324, 2007.

[5] Ulrich, E. R., and Pines, D., "Planform Geometric Variation, and its Effect on the Autorotation Efficiency of Mechanical Samara," *American Helicopter Society 64th Annual Forum*, Vol. 2, AHS International, Alexandria, VA, 2008, p. 1138.

[6] Ulrich, E. R., and Pines, D., "Effects of Planform Geometry on Mechanical Samara Autorotation Efficiency and Rotational Dynamics," *Journal of the American Helicopter Society*, 2010 (to be published).

[7] Ulrich, E. R., Pines, D., and Humbert, J. S., "Pitch and Heave Control of Robotic Samara Micro-Air-Vehicles," *Journal of Aircraft*, Vol. 47, No. 4, 2010, pp. 1290–1299. doi:10.2514/1.47197

[8] Leishman, J. G., *Principals of Helicopter Aerodynamics*, Cambridge Univ. Press, New York, 2006, pp. 160–190.

[9] Klein, V., and Morelli, E., *Aircraft System Identification: Theory and Practice*, AIAA Education Series, AIAA, Reston, VA, 2006, Chap. 4.